Chiral Majorana fermion modes regulated by a scanning tunneling microscope tip

Yan-Feng Zhou,[1,2] Zhe Hou,[1,2] Ying-Tao Zhang,[3] and Qing-Feng Sun[1,2,4,*]

[1]*International Center for Quantum Materials, School of Physics, Peking University, Beijing 100871, China*
[2]*Collaborative Innovation Center of Quantum Matter, Beijing 100871, China*
[3]*College of Physics, Hebei Normal University, Shijiazhuang 050016, China*
[4]*CAS Center for Excellence in Topological Quantum Computation, University of Chinese Academy of Sciences, Beijing 100190, China*

The Majorana fermion can be described by a real wave function with only two phases (zero and π) which provide a controllable degree of freedom. We propose a strategy to regulate the phase of the chiral Majorana state by coupling with a scanning tunneling microscope tip in a system consisting of a quantum anomalous Hall insulator coupled with a superconductor. With the change in the chemical potential, the chiral Majorana state can be tuned alternately between zero and π, in which the perfect normal tunneling and perfect crossed Andreev reflection appear, respectively. The perfect crossed Andreev reflection, by which a Cooper pair can be split into two electrons going into different terminals completely, leads to a pumping current and distinct quantized resistances. These findings may provide a signature of Majorana fermions and pave a feasible avenue to regulate the phase of the Majorana state.

I. INTRODUCTION

Topological superconductors (TSCs), the superconducting counterparts of topological insulators, have attracted more and more attention for catching Majorana fermions in condensed-matter systems [1–5]. The Majorana zero modes exhibiting non-Abelian statistics [1,6,7] can exist in the core of superconducting vortices in the chiral TSCs and have potential applications in topological quantum computation. Exotic effects, such as the 4π-periodic Josephson effect [8,9] and nonlocal tunneling [10–12], could be the promising manifestation of the zero-dimensional Majorana bound states. Theoretical proposals have shown that the chiral TSCs can be realized by inducing superconductivity in quantum Hall systems, quantum anomalous Hall insulators (QAHIs) [13,14], and two-dimensional systems with spin-orbit coupling [15,16] via the proximity effect of an s-wave superconductor. Moreover, there also exist $\mathcal{N}$ one-dimensional chiral Majorana edge modes (CMEMs) in the interface of chiral TSCs with topological Chern number $\mathcal{N}$. Especially, a half-integer conductance plateau at the coercive field in a hybrid TSC/QAHI structure based on the one-dimensional CMEMs has been predicted by theoretical studies [14,17–19] and has been observed recently in a transport experiment [20], providing a transport signature of CMEMs [14,21]. For promising applications of Majorana fermions, it is important to control the Majorana modes in a feasible way and explore more compelling experimental evidence of them in the chiral TSCs [22,23].

The electron-hole conversion can occur at the interface between a superconductor and a conductor, forming a Cooper pair in the superconductor. Here the incoming electron can be reflected as a hole in the same lead, known as local

Andreev reflection (LAR) [24,25], or be scattered to the other lead, known as crossed Andreev reflection (CAR) [26–29]. When bias occurs below the superconductor gap, the transport properties of the system are mainly determined by the Andreev reflections [25,30]. Because of the LAR and other processes, such as normal reflection and normal tunneling, the probability of the CAR is, in general, very small. Recently, some works have focused on the Andreev reflections in the superconductor/topological system, and some exotic phenomena have been predicted [31–41]. For example, a resonant CAR can be obtained with other processes being prohibited through band engineering of the electron/hole in the leads [31–33] or with the assistance of the Majorana end sates [34]. In addition, by utilizing the unidirectionality of the topologically protected edge states, the quantized CAR is proposed in the systems by coupling an s-wave superconductor with a QAHI ribbon [35] and spin-valley topological insulator [36].

In this paper, we propose an avenue to control the phase of the CMEMs in the hybrid TSC/QAHI system by using a scanning tunneling microscope (STM) tip and demonstrate a quantized perfect CAR caused by the phase regulation. Because of the property that the Majorana fermion is a self-Hermitian particle, its wave function is real, and its phase can be only zero or π. Moreover, for a one-dimensional chiral Majorana fermion with propagation velocity v_M obeying the Hamiltonian $H = -i\hbar v_M \partial_x$ [42–44], the current density $j_x = v_M \Psi^* \Psi$, and the wave function Ψ is nonzero at any site due to the current conservation condition. Consequently, the phase of the Majorana fermion γ propagating forward along the CMEM is only zero, i.e., $\gamma \rightarrow \gamma$ [42,43]. However, with the branch cut introduced by the STM tip, the chiral Majorana fermion cannot be regarded as a one-dimensional system any more, leading to the possibility that its phase can be zero or π. We show that the phase can be easily regulated from zero to π, i.e., $\gamma \rightarrow -\gamma$ for the π phase. Corresponding to the zero
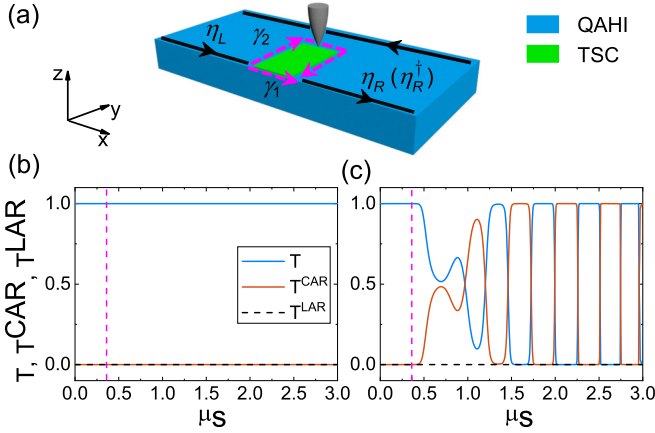
FIG. 1. (a) Schematic diagram of the hybrid TSC/QAHI system coupled by a STM tip. In the green region, a TSC state is induced through the proximity effect by coupling with an s-wave superconductor. The gray tip is the STM tip. Black arrows label the QAHI edge states, and magenta arrows indicate the CMEMs. (b) and (c) The normal tunneling coefficient T, CAR coefficient T^{CAR}, and LAR coefficient T^{LAR} as functions of μ_s without and with the STM tip, respectively. The STM tip coupling strength $\Gamma = 1$, the coupling position is in the middle of the upper edge of the TSC island, and the contact region is 3×3 lattices in the numerical simulation. The QAHI ribbon width $W = 150a$, and the size of the TSC island is $(L_x, L_y) = (20a, 90a)$.

and π phases, perfect normal tunneling and quantized perfect CAR can occur, respectively.

The organization of this paper is as follows. After this introductory section, Sec. II describes the theoretical models of the TSC/QAH system coupled with the STM tip and the methods for calculating the tunneling coefficient, the LAR coefficient, the CAR coefficient, and the current. Section III presents the numerical results of the phase modulation of CMEMs by the STM tip, coherence, and experimental signatures. Section IV concludes this paper. Some auxiliary materials are relegated to the appendixes.

II. MODEL

We consider a hybrid TSC/QAHI system in which a chiral TSC island is introduced near one edge of the QAHI ribbon and a STM tip couples to the TSC island, as shown in Fig. 1(a). In fact, some recent experimental and theoretical works have applied the STM tip to probe the Majorana fermion [22,45,46]. Here we apply it to regulate the phase of the Majorana state propagating forward along the CMEM. The QAHI states have been predicted in some realistic proposals by doping topological insulators with magnetic dopants and have been experimentally realized in Cr-doped [47–51] and V-doped [52] (Bi,Sb)$_2$Te$_3$ magnetic topological insulator thin films. For the low-energy states near the Γ point, the two-band Hamiltonian describing the QAHI state can be expressed as [13] $\mathcal{H}_{\mathrm{QAHI}} = \sum_{\mathbf{p}} \psi_{\mathbf{p}}^{\dagger} H_{\mathrm{QAHI}}(\mathbf{p}) \psi_{\mathbf{p}}$, with $\psi_{\mathbf{p}} = (c_{\mathbf{p}\uparrow}, c_{\mathbf{p}\downarrow})^T$ and

$$H_{\mathrm{QAHI}}(\mathbf{p}) = (m + Bp^2)\sigma_z + A(p_x \sigma_x + p_y \sigma_y), \quad (1)$$

where $c_{\mathbf{p}\sigma}$ and $c_{\mathbf{p}\sigma}^{\dagger}$ are, respectively, the annihilation and creation operators with momentum $\mathbf{p}$ and spin $\sigma = \uparrow, \downarrow$ and $\sigma_{x,y,z}$ are Pauli matrices for spin. A, B, and m are material parameters. For the numerical calculation, the Hamiltonian $\mathcal{H}_{\mathrm{QAHI}}$ can be further mapped into a square lattice model in the tight-binding representation [53],

$$\mathcal{H}_{\mathrm{QAHI}} = \sum_{\mathbf{i}} [\psi_{\mathbf{i}}^{\dagger} T_0 \psi_{\mathbf{i}} + (\psi_{\mathbf{i}}^{\dagger} T_x \psi_{\mathbf{i}+\delta\mathbf{x}} + \psi_{\mathbf{i}}^{\dagger} T_y \psi_{\mathbf{i}+\delta\mathbf{y}}) + \mathrm{H.c.}],$$

$$(2)$$

with $T_0 = (m + 4B\hbar^2/a^2)\sigma_z$, $T_x = -(B\hbar^2/a^2)\sigma_z - (iA\hbar/2a)\sigma_x$, and $T_y = -(B\hbar^2/a^2)\sigma_z - (iA\hbar/2a)\sigma_y$. Here $\psi_{\mathbf{i}} = (c_{\mathbf{i}\uparrow}, c_{\mathbf{i}\downarrow})^T$, and $c_{\mathbf{i}\sigma}$ and $c_{\mathbf{i}\sigma}^{\dagger}$ are, respectively, the annihilation and creation operators on site $\mathbf{i}$ with spin σ. a is the lattice length, and $\delta\mathbf{x}$ ($\delta\mathbf{y}$) is the unit vector along the x (y) direction. The topological properties of the Hamiltonian $\mathcal{H}_{\mathrm{QAHI}}$ are determined by the sign of m/B. For $m/B < 0$, the QAHI state with Chern number $\mathcal{C} = 1$ is obtained, and one chiral edge mode exists at each edge in a QAHI ribbon, as indicated by black arrows in Fig. 1(a). For $m/B > 0$, the Hamiltonian $\mathcal{H}_{\mathrm{QAHI}}$ describes a normal insulator state with Chern number $\mathcal{C} = 0$.

Near one edge of the QAHI ribbon, an s-wave superconductor is coupled to it [see the green region in Fig. 1(a)], and the proximity effect can induce a finite pairing potential Δ in the superconductor-covered QAHI region. In this region, the electron and hole excitations are described by the Bogoliubov–de Gennes (BdG) Hamiltonian, $\mathcal{H}_{\mathrm{BdG}} = \frac{1}{2} \sum_{\mathbf{p}} \Psi_{\mathbf{p}}^{\dagger} H_{\mathrm{BdG}}(\mathbf{p}) \Psi_{\mathbf{p}}$, in the basis of $\Psi_{\mathbf{p}} = (c_{\mathbf{p}\uparrow}, c_{\mathbf{p}\downarrow}, c_{-\mathbf{p}\uparrow}^{\dagger}, c_{-\mathbf{p}\downarrow}^{\dagger})^T$, and

$$H_{\mathrm{BdG}} = \begin{pmatrix} H_{\mathrm{QAHI}}(\mathbf{p}) - \mu_s & i\Delta\sigma_y \\ -i\Delta^*\sigma_y & -H_{\mathrm{QAHI}}^*(-\mathbf{p}) + \mu_s \end{pmatrix}. \quad (3)$$

Here a finite chemical potential μ_s has been taken into account inside the TSC island. Using Eq. (2), the lattice version of Hamiltonian $\mathcal{H}_{\mathrm{BdG}}$ can also be obtained. According to the Altland-Zirnbauer symmetry classification scheme, the Hamiltonian $\mathcal{H}_{\mathrm{BdG}}$, which has intrinsic particle-hole symmetry but no time-reversal symmetry, belongs to the D-class TSC [54]. The D-class TSCs in two dimensions can be described by Chern number $\mathcal{N}$ and support $\mathcal{N}$ CMEMs. According to the phase diagram of the Hamiltonian $\mathcal{H}_{\mathrm{BdG}}$ [13], for a finite superconductor gap Δ and negative m, the TSC region undergoes a phase transition from $\mathcal{N} = 2$ to $\mathcal{N} = 1$ (also called chiral TSC) by changing the chemical potential μ_s, and the phase boundary is determined by the condition $\Delta^2 + \mu_s^2 = m^2$. It is worth noting that here $\mathcal{N} = 2$ CMEMs are topologically equivalent to one QAHI edge state ($\mathcal{C} = 1$). Very recently, the TSC with $\mathcal{N} = 1$ was successfully realized experimentally [20].

Then the Hamiltonian H of the whole setup consisting of the hybrid TSC/QAHI ribbon coupled by a STM tip [see Fig. 1(a)] is

$$H = \mathcal{H}_{\mathrm{QAHI/BdG}} + H_{\mathrm{STM}} + H_{\mathrm{C}}, \quad (4)$$

where $\mathcal{H}_{\mathrm{QAHI/BdG}}$, H_{STM}, and H_{C} are the Hamiltonians of the hybrid TSC/QAHI ribbon, the STM tip, and the coupling between them, respectively. $\mathcal{H}_{\mathrm{QAHI/BdG}}$ is shown in

Eqs. (1)–(3). The Hamiltonians H_{STM} and H_C are

$$H_{\mathrm{STM}} + H_C = \sum_{\mathbf{i},k} (\varepsilon_{\mathbf{i}k} a_{\mathbf{i}k}^\dagger a_{\mathbf{i}k} + t_d a_{\mathbf{i}k}^\dagger \psi_{\mathbf{i}} + \mathrm{H.c.}), \qquad (5)$$

where $a_{\mathbf{i}k} = (a_{\mathbf{i}\uparrow k}, a_{\mathbf{i}\downarrow k})^T$ and $a_{\mathbf{i}\sigma k}$ and $a_{\mathbf{i}\sigma k}^\dagger$ are, respectively, the annihilation and creation operators of the STM tip with spin σ. Here the STM tip couples to only a few **i** sites, and t_d is the coupling strength. The coupling strength is also characterized by $\Gamma = 2\pi\rho t_d^2$, with ρ being the density of states of the STM tip.

Note that here the Hamiltonian of the STM tip is the same as that of a metallic lead. So the effect of the STM tip can be produced by coupling a metallic island to the TSC island in the experiment, and similar results can also be obtained [23]. But in a specific setup, the coupling strength between the metallic island and the TSC island cannot be changed. By contrast, the STM tip is movable, and the coupling strength Γ between the tip and the TSC island can be controlled.

In the numerical calculation, we set $m = -0.5$, $\Delta = 0.35$, and $A = B = 1$ with a regularization lattice constant $a = 1$ and $\hbar = 1$. For an estimation in real materials, $\hbar v_F \sim 260$ meV nm (v_F is Fermi velocity), and the proximity-effect-induced superconductor gap $\Delta = 0.35$ meV [14]. The lattice constant $a = \hbar v_F / A = 0.26$ μm [see Eq. (2)], and the TSC island size $(L_x, L_y) = (20a, 90a) = (5.2 \ \mu\mathrm{m}, 23.4 \ \mu\mathrm{m})$ in Fig. 1(a), where L_x and L_y are the length and width of the TSC island. This size is similar to that of the experiment device [20]. The normal tunneling coefficient T, CAR coefficient T^{CAR}, and LAR coefficient T^{LAR} can be calculated using the nonequilibrium Green's function method combined with the Landauer-Büttiker formula (see Appendix A for details of the calculation [25,53,55–57]).

III. RESULTS

A. Phase modulation by the STM tip

For the case without the STM tip, the normal tunneling coefficient T, CAR coefficient T^{CAR}, and LAR coefficient T^{LAR} in the zero-incident-energy case as functions of the chemical potential μ_s are shown in Fig. 1(b). Here the normal tunneling is perfect with $T = 1$, but T^{CAR}, T^{LAR}, and normal reflection R disappear regardless of the chemical potential μ_s. For $\mu_s < \sqrt{m^2 - \Delta^2}$ [the region to the left of the magenta dashed in Fig. 1(b)], the TSC island is in the $\mathcal{N} = 2$ phase, which is topologically equivalent to the QAHI state. In this case, the incident electron from the left side can be transmitted transparently to the right side. On the other hand, for $\mu_s > \sqrt{m^2 - \Delta^2}$, the TSC island is in the $\mathcal{N} = 1$ phase with a single CMEM. Now when the incident electron η_L along the QAHI edge state from the left side arrives at the interface of the TSC and QAHI, it is separated into two Majorana fermions, γ_1 and γ_2, i.e., $\eta_L = \gamma_1 + i\gamma_2$, with $\gamma_1 = \frac{1}{2}(\eta_L + \eta_L^\dagger)$ and $\gamma_2 = \frac{1}{2i}(\eta_L - \eta_L^\dagger)$. Then γ_1 and γ_2 propagate forward along the lower and upper CMEMs, respectively, indicated by the magenta arrows in Fig. 1(a). Notice that the TSC island does not touch the upper edge of the QAHI ribbon [Fig. 1(a)], so γ_1 and γ_2 must meet at the bottom right corner of the TSC island, and they combine into an ordinary fermion again to the right QAHI terminal. Due to the reality constraint on

the wave function of the one-dimensional CMEM, when the Majorana fermion propagates forward along the CMEM, it cannot change its sign; that is, its phase can be only zero, with $\gamma_1 \to \gamma_1$ and $\gamma_2 \to \gamma_2$ [42,43]. This means that the outgoing particle is $\gamma_1 + i\gamma_2 = \eta_R$, which is an electron. Therefore, the normal tunneling coefficient $T = 1$ and all other processes also disappear in the chiral TSC phase.

In order to regulate the phase of the Majorana state, an STM tip is coupled to one edge of the TSC island [see Fig. 1(a)], which can break the one-dimensional channel behavior due to the branch. Now the phase can be zero or π, and the outgoing upper Majorana state can be γ_2 or $-\gamma_2$, which depends on the chemical potential μ_s. When $\gamma_2 \to \gamma_2$, the outgoing particle $\eta_R = \gamma_1 + i\gamma_2$ is an electron; then the quantized perfect normal tunneling occurs with $T = 1$ and $T^{\mathrm{CAR}} = T^{\mathrm{LAR}} = R = 0$. On the other hand, while $\gamma_2 \to -\gamma_2$, the outgoing particle is a hole: $\gamma_1 - i\gamma_2 = \eta_R^\dagger$. The occurrence of the perfect electron-hole conversion leads to the quantized perfect CAR effect. In this situation, the CAR coefficient T^{CAR} is 1, and all other processes (including the normal tunneling, normal reflection, and LAR) are completely suppressed. Figure 1(c) shows the normal tunneling coefficient T, CAR coefficient T^{CAR}, and LAR coefficient T^{LAR} versus the chemical potential μ_s with the coupling of the STM tip. As expected, with the increase in μ_s, T and T^{CAR} appear alternately as plateaus, with the plateau values being 1 in the chiral TSC regime. Here both normal reflection and LAR completely disappear because the TSC island does not touch the upper edge of the QAHI ribbon, so $T + T^{\mathrm{CAR}} = 1$. When $T^{\mathrm{CAR}} = 0$, the normal tunneling coefficient $T = 1$, which corresponds to the perfect tunneling. However, when $T = 0$, the CAR coefficient $T^{\mathrm{CAR}} = 1$, which is the quantized perfect CAR. That is to say, under the coupling of the STM tip the phase of the Majorana state can be adjusted to zero or π by tuning the chemical potential μ_s, which provides a different way to introduce the branch cut from the interferometry of Majorana fermions by the superconducting vortex [42,43].

Next, we study the effect of the coupling strength Γ of the STM tip on T and T^{CAR}. Here we consider the current at the STM tip terminal to be zero; that is, the STM tip terminal is open. Figure 2(a) shows the normal tunneling coefficient T and CAR coefficient T^{CAR} versus coupling strength Γ under several chemical potentials μ_s which are at the centers of the $T = 1$ plateaus [see Fig. 1(c)]. T remains unity, and T^{CAR} is always zero when increasing Γ from zero, indicating that at these μ_s the phase of the Majorana state is zero and the perfect tunneling occurs regardless of the coupling of the STM tip. More interestingly, for other chemical potentials μ_s located at the centers of the $T^{\mathrm{CAR}} = 1$ plateaus, the normal tunneling coefficient T and CAR coefficient T^{CAR} are strongly affected by the coupling of the STM tip [see Fig. 2(b)]. When the coupling strength $\Gamma = 0$, $T = 1$ and $T^{\mathrm{CAR}} = 0$, which corresponds to the perfect tunneling. With an increase in Γ, the normal tunneling coefficient T reduces from 1 to 0, and the CAR coefficient T^{CAR} increases from 0 to 1 rapidly. T reaches 0 and T^{CAR} is 1 even for a very small Γ (e.g., 0.001), which is the quantized perfect CAR effect. This means that by the coupling of the STM tip, the phase of the Majorana state propagating along the CMEM can be regulated from zero to π, and the perfect tunneling can be changed into the perfect
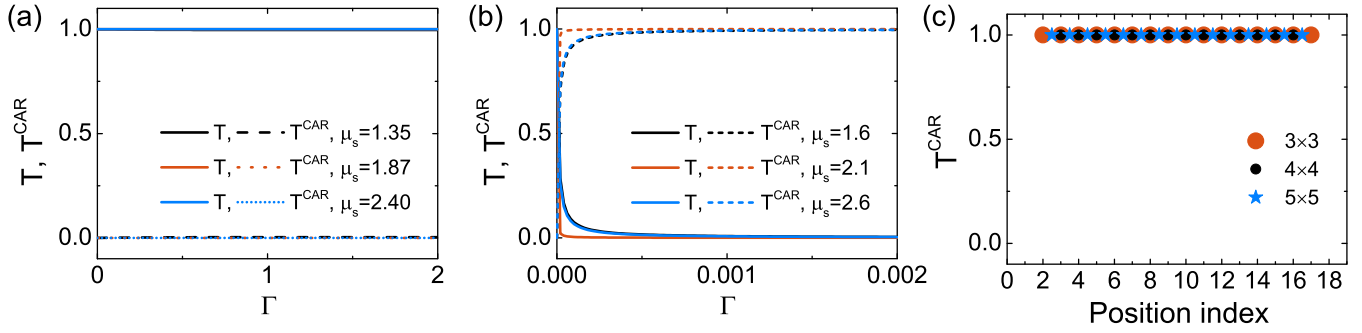
FIG. 2. (a) and (b) The normal tunneling coefficient T and CAR coefficient T^{CAR} versus the coupling strength Γ of the STM tip for several chemical potentials μ_s. The μ_s in (a) and (b) are, respectively, the centers of the $T = 1$ plateaus and the $T^{CAR} = 1$ plateaus in Fig. 1(c). In (a) the three solid curves overlap, and so do the three dotted curves. (c) T^{CAR} versus the coupling position of the STM tip with the different tip sizes and $\mu_s = 2.1$. Here the position index from 0 to 19 means from left to right along the upper edge of the TSC island [see Fig. 1(a)]. The other unmentioned parameters are the same as in Fig. 1(c).

CAR. With a further increase in Γ, the perfect CAR can easily remain with $T^{CAR} = 1$ and $T = 0$.

Let us study the effect of the position of the STM tip on the perfect CAR. Figure 2(c) shows the CAR coefficient T^{CAR} versus the coupling position of the STM tip with several coupling sizes. Here the coupling size of the STM tip $n \times n$ (with $n = 3, 4$, and 5) means that there are $n \times n = n^2$ sites in the TSC/QAHI ribbon coupled to the STM tip. From Fig. 2(c), we can see that $T^{CAR} = 1$ always regardless of the coupling position and the size of the STM tip. That is, the perfect CAR can always take place and is robust against the coupling position and the size of the STM tip. It is worth mentioning that the size of the STM tip usually is very small in general STM spectroscopy experiments. However, the size of the present setup is on the micrometer level [20]. So the size of the STM tip is also required to be large, e.g., about 100 nm or larger. Usually, a large STM tip should be easy to realize experimentally.

Let us study the effect of the size of the TSC island on the regulation of the phase of the Majorana state and quantized perfect CAR. Figure 3 shows T, T^{CAR}, and T^{LAR} as functions

of μ_s for different sizes of the TSC island. As the length L_x and width L_y of the TSC island change, the $T = 1$ plateaus and $T^{CAR} = 1$ plateaus easily remain, and they still appear alternately. That is, the perfect tunneling and the perfect CAR effect can occur regardless of the size of the TSC island. The longer the length L_x of the TSC island is, the more frequent the alternation between the perfect tunneling and perfect CAR is. Moreover, Fig. 4 shows the switching period of T^{CAR} with respect to μ_s as a function of the length L_x of the TSC island. It can be seen that the period is linearly determined by L_x. On the other hand, without the coupling of the STM tip, $T = 1$ and $T^{CAR} = T^{LAR} = 0$ always, as shown in Fig. 1(b), no matter what μ_s and the TSC island size are. This indicates that the coupling of the STM tip can regulate well the phase of the Majorana state from zero to π, which is independent of the size of the TSC island.

In addition, we also study the effect of the TSC gap Δ and the chemical potential μ_{QAHI} of the QAHI region on the regulation of the phase of the Majorana state and the perfect CAR. The perfect tunneling and perfect CAR can always survive as long as μ_{QAHI} is in the bulk gap of the QAHI region, and they can also hold over a wide range of the TSC gap Δ. Hence, the
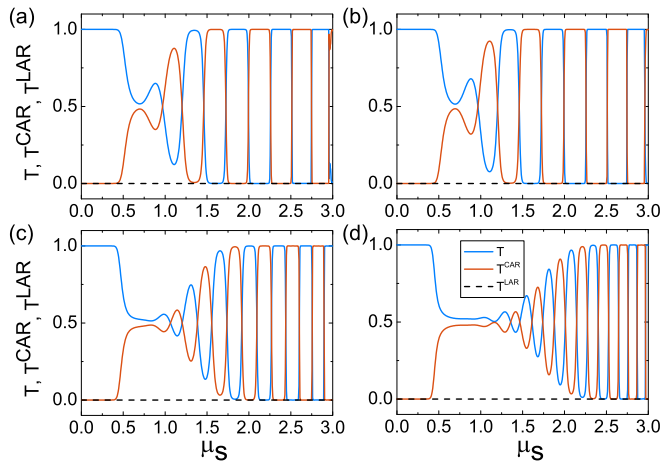

FIG. 3. T, T^{CAR}, and T^{LAR} versus μ_s for the different sizes of the TSC island, (a) $(L_x, L_y) = (20a, 80a)$ (b) $(L_x, L_y) = (20a, 100a)$, (c) $(L_x, L_y) = (30a, 90a)$, and (d) $(L_x, L_y) = (40a, 90a)$, with L_x and L_y being the length and width of the TSC island. All the unmentioned parameters are the same as in Fig. 1(c).
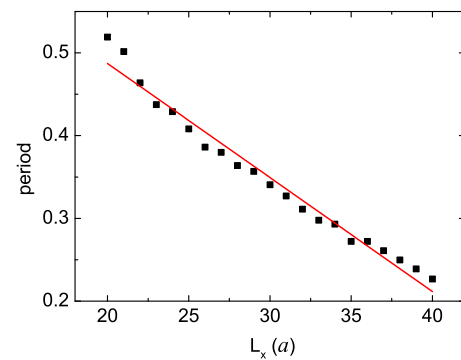

FIG. 4. The switching period of the T^{CAR} with respect to μ_s as a function of the length L_x of the TSC island. The black solid squares are extracted from the curves of the CAR coefficient versus μ_s, and the red solid line is the linear regression for the discrete black solid squares. All the unmentioned parameters are the same as in Fig. 1(c).
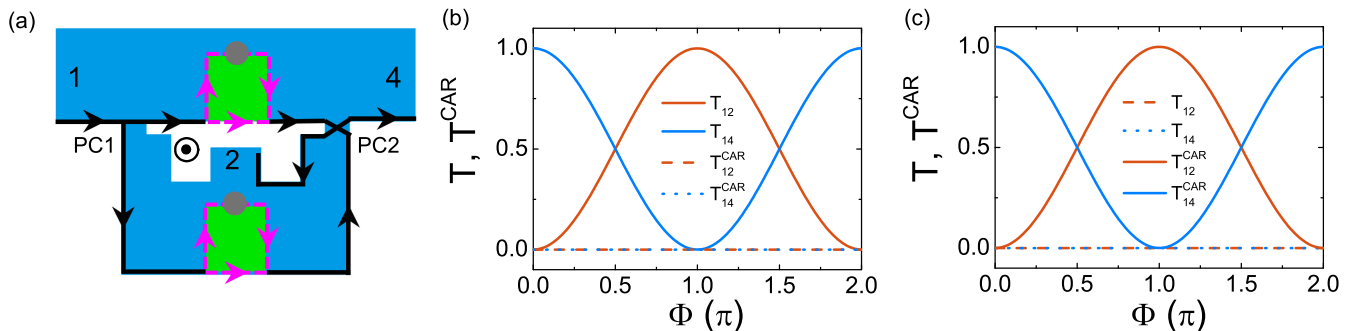
FIG. 5. (a) The configuration of the electronic Mach-Zehnder interferometer. PC1 and PC2 are two point contacts connecting the two TSC/QAHI junctions, and a magnetic flux Φ is threaded in the cavity. The widths of terminals 1, 2, and 4 are $150a$, $70a$, and $150a$, respectively, and the size of the lower TSC/QAHI junction is $(20a, 90a)$. T_{1n} and T_{1n}^{CAR} from terminal 1 to terminal n ($n = 2,4$) as functions of Φ with (b) $\mu_s = 1.87$ and (c) 2.1, which correspond to the perfect tunneling and perfect CAR regimes. All the other unmentioned parameters are the same as Fig. 1(c).

perfect CAR should easily be observed in the experiment, and it can be solid proof for the existence of CMEM.

B. Coherence

With the coupling of the STM tip, the electron and hole may go into and then come back from the STM tip, which is akin to Büttiker virtual probes. Can the STM tip cause the dephasing? Next, we study whether the outgoing electrons or holes remain coherent by using an electronic Mach-Zehnder interferometer with two point contacts (PC1 and PC2), as shown in Fig. 5(a) [58]. In the PCs, by fine-tuning the coupling strength, an incident electron is equally transmitted to two paths, similar to beam splitters. Two TSC islands are introduced in the transmission paths of the interferometer, and a magnetic flux Φ is threaded in the cavity. PC1 splits the incoming edge current from terminal 1 into two paths. After crossing the TSC islands, they recombine again in PC2 and finally go to terminals 2 and 4. Figures 5(b) and 5(c) show the normal tunneling coefficient T_{1n} and CAR coefficient T_{1n}^{CAR} ($n = 2,4$) from terminal 1 to terminal n as functions of magnetic flux Φ, which introduces a phase difference between the two paths via the Aharonov-Bohm effect. In the parameter regimes in Figs. 5(b) and 5(c), there are occurrences of the perfect tunneling and perfect CAR in the region of the TSC/QAHI junction, with the outgoing particles being electrons and holes, respectively. As shown in Fig. 5(b) [Fig. 5(c)], the normal tunneling coefficient T_{1n} (the CAR coefficient T_{1n}^{CAR}) oscillates between 0 and 1 with the increase in the magnetic flux Φ, but $T_{12} + T_{14} = 1$ and $T_{12}^{CAR} = T_{14}^{CAR} = 0$ ($T_{12}^{CAR} + T_{14}^{CAR} = 1$ and $T_{12} = T_{14} = 0$). Because the oscillating amplitudes of T_{1n} and T_{1n}^{CAR} equal 1, the electron and hole scattered off the TSC island are still completely coherent despite the coupling of the STM tip. The survival of the phase coherence results from the fact that the Majorana state propagating forward along the CMEMs can take only a phase of zero or π, and the phase cannot be changed randomly by the coupling of the STM tip [59].

C. Experimental signature

Finally, we study the physically observable quantities caused by the perfect CAR and the adjustment of the phase of the Majorana state. We consider a six-terminal Hall bar, as

shown in Fig. 6(a). Here the TSC and lead 4 are grounded, and a small bias V is applied to lead 1, with $V_s = V_4 = 0$ and $V_1 = V$. The other leads are the voltage probes with zero current. Without the coupling of the STM tip, the perfect normal tunnelings occur along the QAHI edge and the CMEM with $T^{CAR} = T^{LAR} = 0$, as shown in Fig. 1(b). In this case, the transport properties are completely the same as those of the quantum anomalous Hall effect, with $V_2 = V_3 = V_4 = 0$, $V_5 = V_6 = V_1 = V$, $I_1 = -I_4 = (e^2/\hbar)V$, longitudinal resistances $V_{23}/I_1 = V_{65}/I_1 = 0$, and Hall resistances $V_{62}/I_1 = V_{53}/I_1 = \hbar/e^2$ regardless of the chemical potential μ_s, where $V_{nm} \equiv V_n - V_m$. However, with the coupling of the STM tip, the results are essentially different, and the observable quantities mentioned above are strongly dependent on the chemical potential μ_s, as shown in Figs. 6(b)–6(d). Now the perfect tunneling and perfect CAR occur alternately when the TSC island is in the chiral TSC phase with $\mathcal{N} = 1$. For the perfect tunneling, the results are the same as above. But for the perfect CAR, the voltage of lead 5 is $V_5 = -V$ instead
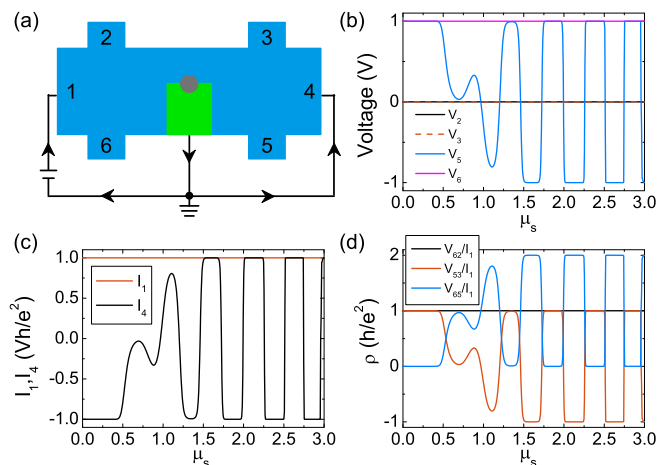

FIG. 6. (a) Schematic diagram of a six-terminal Hall bar system consisting of the QAHI and TSC. (b) The voltages V_n, (c) the currents I_1 and I_4, and (d) the longitudinal and Hall resistances as functions of μ_s. The widths of leads 2, 3, 5, and 6 are $70a$, and all the unmentioned parameters are the same as in Fig. 1(c).

of V [see Fig. 6(b)] because the CAR coefficient $T^{\text{CAR}} = 1$. Notice that V_5 is negative and lower than the voltages of leads 1 and 4, so a pumping current will be driven. The current $I_4 = I_1 = (e^2/\hbar)V$, as shown in Fig. 6(c), in which the currents at both leads 1 and 4 flow into the center region. As there is no external power in the right circuit loop consisting of lead 4 and the superconductor lead in Fig. 6(a), this is a pumping current, where the electrons in lead 1 draw those in lead 4 to combine into Cooper pairs and eventually enter the superconductor lead. The longitudinal resistance of the upper edge $V_{23}/I_1 = 0$, which is independent of μ_s because of the unidirectionality of the QAHI edge states. Nevertheless, the longitudinal conductance of the lower edge $I_1/V_{65} = \frac{1}{2}e^2/h$ at the half-integer quantized value [Fig. 6(d)] due to the occurrence of the perfect CAR. The left Hall resistance $V_{62}/I_1 = h/e^2$, but the right Hall resistance $V_{53}/I_1 = h/e^2$ for the perfect tunneling and $-h/e^2$ for the perfect CAR [see Fig. 6(d)]. These results give solid proof of the CMEM. Moreover, considering that the proposed setup is very similar to the one in the recent experiment [20], the predicted perfect CAR should be experimentally observed with current technologies.

In a realistic experiment involving the STM tip, the voltage and conductance of the STM tip will be there for direct readout whether or not signatures of the phase adjustment from these experimental measurements exist. We calculate both the voltage V_{tip} of the STM tip with its current being zero and the conductance dI_{tip}/dV at the zero voltage $V_{\text{tip}} = 0$. The results show that the voltage V_{tip} and the conductance dI_{tip}/dV are zero for both $T = 1$ and $T^{\text{CAR}} = 1$ phases, but nonzero V_{tip} and dI_{tip}/dV appear at the transitions between $T = 1$ and $T^{\text{CAR}} = 1$ (see Appendix B). This means that the measurements from the STM tip can only manifest the transition between the two phases and cannot distinguish them.

IV. CONCLUSION

In summary, we have studied the effect of a STM tip on the chiral Majorana edge modes and have demonstrated that the phase of the Majorana states can be regulated by the coupling of the STM tip. When a π phase is introduced for the Majorana state, a perfect CAR occurs, and all other scattering processes completely disappear. Moreover, the outgoing electrons and holes can maintain phase coherence well despite the STM tip. The physically observable consequences from the perfect CAR were also studied in a six-terminal Hall bar setup, in which the longitudinal and Hall resistances showed the quantized plateaus. These findings give undoubtable proof of the existence of the chiral Majorana edge mode and open an avenue to control the phase of the Majorana state.

ACKNOWLEDGMENTS

APPENDIX A: DERIVATION OF THE TRANSPORT FORMULA

By using the nonequilibrium Green's function method, the normal tunneling, CAR, and LAR coefficients can be obtained from [55,56]

$$\tilde{T}_{nm}(E) = \text{Tr}[\Gamma_{ee}^n \mathbf{G}_{ee}^r \Gamma_{ee}^m \mathbf{G}_{ee}^a],$$

$$\tilde{T}_{nm}^A(E) = \text{Tr}[\Gamma_{ee}^n \mathbf{G}_{eh}^r \Gamma_{hh}^m \mathbf{G}_{he}^a], \tag{A1}$$

where e and h represent the electron and hole, respectively, E is the incident energy, and n and m are the indices of the terminals, including the left and right terminals in Fig. 1(a), terminal n ($n = 1, 2, \ldots, 6$) in Fig. 6(a), and the STM tip terminal. $\mathbf{G}^r(E) = [E - \mathcal{H}_{\text{BdG}} - \sum_n \Sigma_n^r]^{-1}$ is the retarded Green's function, where $\mathcal{H}_{\text{BdG}}$ is the BdG Hamiltonian of the central region. $\Gamma^n(E) = i[\Sigma_n^r - \Sigma_n^a]$ is the linewidth function. The self-energy $\Sigma_n^r = \Sigma_n^{a\dagger}$ stems from the coupling between terminal n and the center regions. For the QAHI terminal, the self-energy can be calculated numerically [57]. However, for the STM tip terminal, $\Sigma_{\text{tip}}^r = -\frac{i\Gamma}{2}\mathbf{I}_{4N}$, where $\Gamma = 2\pi\rho t_d^2$ is the coupling strength between the STM tip and the TSC island, $\mathbf{I}_{4N}$ is the $4N \times 4N$ unit matrix in the BdG representation, and N is the number of sites coupled with the STM tip. In Eq. (A1), $\tilde{T}_{nm}(E)$ ($n \neq m$) is the normal tunneling coefficient from terminal n to terminal m, and $\tilde{T}_{nm}^A(E)$ is the Andreev reflection coefficient. For $n \neq m$, $\tilde{T}_{nm}^A$ is the CAR coefficient, while for $n = m$ it is the LAR coefficient. Because there is only one edge mode in the QAHI terminal, the normal reflection coefficient for the QAHI terminal is $\tilde{R}_{nn} = 1 - \sum_{m(m \neq n)} \tilde{T}_{nm} - \sum_m \tilde{T}_{nm}^A$.

After these transmission coefficients are obtained, the current in terminal n at the small-bias limit can be calculated using the multiprobe Landauer-Büttiker formula [25],

$$I_n = (e^2/h)\left[(V_n - V_s)\tilde{T}_{sn}(0) + \sum_{m(m \neq n)} (V_n - V_m)\tilde{T}_{mn}(0) \right.$$

$$\left. + 2V_n\tilde{T}_{nn}^A(0) + \sum_{m(m \neq n)} (V_n + V_m)\tilde{T}_{mn}^A(0) \right], \tag{A2}$$

where V_n is the voltage of terminal n. Here the voltage V_s of the superconductor lead is set to zero. When the incident energy $E = 0$, which is inside the superconductor gap, the tunneling coefficient $\tilde{T}_{sn}$ between terminal n and the superconductor lead is zero, so the first term in Eq. (A2) vanishes. For the voltage terminals [e.g., the STM tip and terminals 2, 3, 5, and 6 in Fig. 6(a)], the currents are zero, and their voltage can be solved with Eq. (A2).

We take the system in Fig. 1(a) as an example. Setting the voltages V_L and V_R for the left and right QAHI terminals and $I_{\text{tip}} = 0$ in the STM tip, the currents I_L and I_R and voltage V_{tip} can easily be solved using Eq. (A2), and they are linearly dependent on V_L and V_R. For example, the current in the right terminal can be written as $I_R = (e^2/h)(a_R V_R + a_L V_L) = (e^2/h)[\frac{a_R + a_L}{2}(V_R + V_L) + \frac{a_R - a_L}{2}(V_R - V_L)]$. Here the coefficients $\frac{a_R - a_L}{2}$ ($\frac{a_R + a_L}{2}$) of $V_R - V_L$ ($V_R + V_L$) represent the probability of the outgoing electron (hole), which is the total normal tunneling coefficient T (total CAR coefficient T^{CAR}), including the direct tunneling from L to R, the indirect process

from L passing the STM tip to R, and so on. In addition, the LAR coefficient $T^{\text{LAR}} = \tilde{T}^A_{R,R}$, and the normal reflection $R = 1 - T - T^{\text{CAR}} - T^{\text{LAR}}$. Both of them are zero because of the absence of touching between the TSC island and the upper edge of the QAHI ribbon [see Fig. 1(a)].

APPENDIX B: VOLTAGE AND CONDUCTANCE OF THE STM TIP

Let us study both the voltage V_{tip} of the STM tip while its current is zero and the conductance dI_{tip}/dV at the zero voltage $V_{\text{tip}} = 0$. Here the setup shown in Fig. 1(a) is considered. The voltage of the left QAHI terminal sets V, and the voltages of the TSC island and the right QAHI terminal are zero. For the STM tip terminal, two boundary conditions are considered: (1) The current of the STM tip is set to zero (i.e., the open-circuit condition), and the voltage V_{tip} of the STM tip is studied. (2) The voltage V_{tip} is zero (i.e., ground), and the conductance dI_{tip}/dV is investigated.

Figure 7 shows the voltage V_{tip} and the conductance dI_{tip}/dV as a function of the chemical potential μ_s. Here the parameters are the same as in Fig. 1(c). The voltage V_{tip} and the conductance dI_{tip}/dV are zero for both $T = 1$ and $T^{\text{CAR}} = 1$ phases. But nonzero V_{tip} and dI_{tip}/dV appear at the transitions between $T = 1$ and $T^{\text{CAR}} = 1$. These results are very consistent with the physical picture of the one-dimensional CMEMs shown in Fig. 1(a). From the one-dimensional CMEMs in Fig. 1(a), we can see that only the Majorana fermion γ_2 [$\gamma_2 = \frac{1}{2i}(\eta_L - \eta_L^\dagger)$] can tunnel into the STM tip. So the normal tunneling and Andreev reflection coefficients are $\tilde{T}_{L,\text{tip}} = \tilde{T}^A_{L,\text{tip}} = |c|^2/4$ and $\tilde{T}_{R,\text{tip}} = \tilde{T}^A_{R,\text{tip}} = 0$,
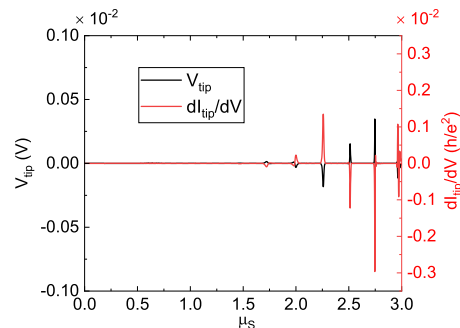

FIG. 7. The voltage of the STM tip V_{tip} and the conductance dI_{tip}/dV as a function of μ_s. The voltage V_{tip} is calculated under the open-circuit condition with the STM tip current $I_{\text{tip}} = 0$. The conductance dI_{tip}/dV is calculated at $V_{\text{tip}} = 0$. The voltage $V_L = V$, and $V_R = V_s = 0$. The parameters are the same as in Fig. 1(c).

where c is the tunneling amplitude from γ_2 to the STM tip. c is positive for the $T = 1$ phase and negative for the $T^{\text{CAR}} = 1$ phase. Then from multiprobe Landauer-Büttiker formula, we have

$$
\begin{aligned}
I_{\text{tip}} &= (e^2/h)\Big[(V_{\text{tip}} - V_L)\tilde{T}_{L,\text{tip}} + 2V_{\text{tip}}\tilde{T}^A_{\text{tip,tip}} \\
&\quad + (V_{\text{tip}} + V_L)\tilde{T}^A_{L,\text{tip}}\Big] \\
&= 2(e^2/h)V_{\text{tip}}\Big(\tilde{T}^A_{\text{tip,tip}} + |c|^2/4\Big).
\end{aligned} \tag{B1}
$$

So the tip voltage V_{tip} is zero under the open-circuit condition with the current $I_{\text{tip}} = 0$, and the current $I_{\text{tip}} = 0$ (i.e., the conductance $dI_{\text{tip}}/dV = 0$) when the tip is grounded with $V_{\text{tip}} = 0$.

[1] N. Read and D. Green, Phys. Rev. B **61**, 10267 (2000).
[2] X.-L. Qi and S.-C. Zhang, Rev. Mod. Phys. **83**, 1057 (2011).
[3] J. Alicea, Rep. Prog. Phys. **75**, 076501 (2012).
[4] C. W. J. Beenakker, Annu. Rev. Condens. Matter Phys. **4**, 113 (2013).
[5] S. R. Elliott and M. Franz, Rev. Mod. Phys. **87**, 137 (2015).
[6] D. A. Ivanov, Phys. Rev. Lett. **86**, 268 (2001).
[7] C. Nayak, S. H. Simon, A. Stern, M. Freedman, and S. Das Sarma, Rev. Mod. Phys. **80**, 1083 (2008)
[8] L. Fu and C. L. Kane, Phys. Rev. B **79**, 161408 (2009).
[9] R. M. Lutchyn, J. D. Sau, and S. Das Sarma, Phys. Rev. Lett. **105**, 077001 (2010).
[10] J. Nilsson, A. R. Akhmerov, and C. W. J. Beenakker, Phys. Rev. Lett. **101**, 120403 (2008).
[11] K. T. Law, P. A. Lee, and T. K. Ng, Phys. Rev. Lett. **103**, 237001 (2009).
[12] Z. Wang, X.-Y. Hu, Q.-F. Liang, and X. Hu, Phys. Rev. B **87**, 214513 (2013).
[13] X.-L. Qi, T. L. Hughes, and S.-C. Zhang, Phys. Rev. B **82**, 184516 (2010).
[14] J. Wang, Q. Zhou, B. Lian, and S.-C. Zhang, Phys. Rev. B **92**, 064520 (2015).
[15] L. Fu and C. L. Kane, Phys. Rev. Lett. **100**, 096407 (2008).
[16] J. D. Sau, R. M. Lutchyn, S. Tewari, and S. Das Sarma, Phys. Rev. Lett. **104**, 040502 (2010).

[17] S. B. Chung, X.-L. Qi, J. Maciejko, and S.-C. Zhang, Phys. Rev. B **83**, 100512 (2011).
[18] B. Lian, J. Wang, and S.-C. Zhang, Phys. Rev. B **93**, 161401 (2016).
[19] J. Wang, Phys. Rev. B **94**, 214502 (2016).
[20] Q. L. He, L. Pan, A. L. Stern, E. C. Burks, X. Che, G. Yin, J. Wang, B. Lian, Q. Zhou, E. S. Choi, K. Murata, X. Kou, Z. Chen, T. Nie, Q. Shao, Y. Fan, S.-C. Zhang, K. Liu, J. Xia, and K. L. Wang, Science **357**, 294 (2017).
[21] C.-Z. Chen, J. J. He, D.-H. Xu, and K. T. Law, Phys. Rev. B **96**, 041118 (2017).
[22] G. C. Ménard, S. Guissart, Ch. Brun, R. T. Leriche, M. Trif, F. Debontridder, D. Demaille, D. Roditchev, P. Simon, and T. Cren, Nat. Commun. **8**, 2040 (2017).
[23] R. P. Tiwari, U. Zülicke, and C. Bruder, New J. Phys. **16**, 025004 (2014).
[24] A. F. Andreev, Zh. Eksp. Teor. Fiz. **46**, 1823 (1964) [Sov. Phys. JETP **19**, 1228 (1964)].
[25] Q.-F. Sun, J. Wang, and T.-H. Lin, Phys. Rev. B **59**, 3831 (1999).
[26] J. M. Byers and M. E. Flatté, Phys. Rev. Lett. **74**, 306 (1995).
[27] G. Deutscher and D. Feinberg, Appl. Phys. Lett. **76**, 487 (2000).
[28] Z. Hou, Y. Xing, A.-M. Guo, and Q.-F. Sun, Phys. Rev. B **94**, 064516 (2016); Y.-T. Zhang, X. Deng, Q.-F. Sun, and Z. Qiao, Sci. Rep. **5**, 14892 (2015).

[29] P. Recher, E. V. Sukhorukov, and D. Loss, Phys. Rev. B **63**, 165314 (2001).

[30] Q.-F. Sun, H. Guo, and T.-H. Lin, Phys. Rev. Lett. **87**, 176601 (2001).

[31] W. Chen, R. Shen, L. Sheng, B. G. Wang, and D. Y. Xing, Phys. Rev. B **84**, 115420 (2011).

[32] M. Veldhorst and A. Brinkman, Phys. Rev. Lett. **105**, 107002 (2010).

[33] J. Cayssol, Phys. Rev. Lett. **100**, 147001 (2008).

[34] J. J. He, J. Wu, T.-P. Choy, X.-J. Liu, Y. Tanaka, and K. T. Law, Nat. Commun. **5**, 3232 (2014).

[35] Y. T. Zhang, Z. Hou, X. C. Xie, and Q.-F. Sun, Phys. Rev. B **95**, 245433 (2017).

[36] J. Wang, L. Hao, and K. S. Chan, Phys. Rev. B **91**, 085415 (2015).

[37] C. Schrade, A. A. Zyuzin, J. Klinovaja, and D. Loss, Phys. Rev. Lett. **115**, 237001 (2015); C. Reeg, J. Klinovaja, and D. Loss, Phys. Rev. B **96**, 081301 (2017).

[38] C. Benjamin and J. K. Pachos, Phys. Rev. B **81**, 085101 (2010).

[39] Q.-F. Sun, Y.-X. Li, W. Long, and J. Wang, Phys. Rev. B **83**, 115315 (2011).

[40] Z. Hou and Q.-F. Sun, Phys. Rev. B **96**, 155305 (2017).

[41] K. Zhang, J. Zeng, Y. Ren, and Z. Qiao, Phys. Rev. B **96**, 085117 (2017).

[42] L. Fu and C. L. Kane, Phys. Rev. Lett. **102**, 216403 (2009).

[43] A. R. Akhmerov, J. Nilsson, and C. W. J. Beenakker, Phys. Rev. Lett. **102**, 216404 (2009).

[44] S. Park, J. E. Moore, and H.-S. Sim, Phys. Rev. B **89**, 161408 (2014).

[45] H.-H. Sun, K.-W. Zhang, L.-H. Hu, C. Li, G.-Y. Wang, H.-Y. Ma, Z.-A. Xu, C.-L. Gao, D.-D. Guan, Y.-Y. Li, C. Liu, D. Qian, Y. Zhou, L. Fu, S.-C. Li, F.-C. Zhang, and J.-F. Jia, Phys. Rev. Lett. **116**, 257003 (2016); L.-H. Hu, C. Li, D.-H. Xu, Y. Zhou, and F.-C. Zhang, Phys. Rev. B **94**, 224501 (2016).

[46] P. Devillard, D. Chevallier, and M. Albert, Phys. Rev. B **96**, 115413 (2017).

[47] C.-Z. Chang, J. Zhang, X. Feng, J. Shen, Z. Zhang, M. Guo, K. Li, Y. Ou, P. Wei, L.-L. Wang, Z.-Q. Ji, Y. Feng, S. Ji, X. Chen, J. Jia, X. Dai, Z. Fang, S.-C. Zhang, K. He, Y. Wang, L. Lu, X.-C. Ma, and Q.-K. Xue, Science **340**, 167 (2013).

[48] J. G. Checkelsky, R. Yoshimi, A. Tsukazaki, K. S. Takahashi, Y. Kozuka, J. Falson, M. Kawasaki, and Y. Tokura, Nat. Phys. **10**, 731 (2014).

[49] X. Kou, S.-T. Guo, Y. Fan, L. Pan, M. Lang, Y. Jiang, Q. Shao, T. Nie, K. Murata, J. Tang, Y. Wang, L. He, T.-K. Lee, W.-L. Lee, and K. L. Wang, Phys. Rev. Lett. **113**, 137201 (2014).

[50] A. J. Bestwick, E. J. Fox, X. Kou, L. Pan, K. L. Wang, and D. Goldhaber-Gordon, Phys. Rev. Lett. **114**, 187201 (2015).

[51] A. Kandala, A. Richardella, S. Kempinger, C.-X. Liu, and N. Samarth, Nat. Commun. **6**, 7434 (2015).

[52] C.-Z. Chang, W. Zhao, D. Y. Kim, H. Zhang, B. A. Assaf, D. Heiman, S.-C. Zhang, C. Liu, M. H. W. Chan, and J. S. Moodera, Nat. Mater. **14**, 473 (2015).

[53] S. Datta, *Electronic Transport in Mesoscopic System* (Cambridge University Press, Cambridge, 1995).

[54] A. P. Schnyder, S. Ryu, A. Furusaki, and A. W. W. Ludwig, Phys. Rev. B **78**, 195125 (2008).

[55] Q.-F. Sun and X. C. Xie, J. Phys.: Condens. Matter **21**, 344204 (2009).

[56] S.-G. Cheng, Y. Xing, J. Wang, and Q.-F. Sun, Phys. Rev. Lett. **103**, 167003 (2009).

[57] D. H. Lee and J. D. Joannopoulos, Phys. Rev. B **23**, 4997 (1981).

[58] Y. Ji, Y. Chung, D. Sprinzak, M. Heiblum, D. Mahalu, and H. Shtrikman, Nature (London) **422**, 415 (2003).

[59] Some other potential sources of decoherence inevitably exist in real experiments. As the Majorana fermions are charge-neutral particles, the coupling of the Majorana fermion with the surrounding environment would be weak, and the dephasing from them is neglectable. Moreover, the dephasing effect of the interaction within the Majorana fermions will be suppressed to a great extent at low temperature [42]. For these reasons, the effects of these dephasing processes are not considered here.